

Triaxial deformation and the loss of the $N = 28$ shell gap

Y. Suzuki

Department of Physics, Hokkaido University, 060-0810 Sapporo, Japan

M. Kimura*

Department of Physics, Hokkaido University, Sapporo 060-0810, Japan

Nuclear Reaction Data Centre, Hokkaido University, Sapporo 060-0810, Japan and

Research Center for Nuclear Physics (RCNP),

Osaka University, Ibaraki 567-0047, Japan

(Dated: March 11, 2021)

Abstract

Background: Recent accumulation of experimental data is revealing the nuclear deformation in vicinity of ^{42}Si . This requests systematic theoretical studies to clarify more specific aspects of nuclear deformation and its causes.

Purpose: The purpose of this study is to investigate the nature and cause of the nuclear deformations and its relation to the loss of the neutron magic number $N = 28$ in vicinity of ^{42}Si .

Method: The framework of antisymmetrized molecular dynamics with Gogny D1S density functional has been applied. The model assumes no spatial symmetry and can describe triaxial deformation. It also incorporates with the configuration mixing by the generator coordinate method.

Results: We show that the shell effects and the loss of the magicity induce various nuclear deformations. In particular, the $N = 26$ and $N = 30$ isotones have triaxially deformed ground states. We also note that the erosion of the $N = 28$ magicity gradually occurs and has no definite boundaries.

Conclusion: The present calculation predicts various nuclear deformations in vicinity of ^{42}Si , and suggests that the inter-band electric transitions are good measure for it. We also remark that the magicity is lost without the single-particle level inversion in the oblate deformed nuclei such as ^{42}Si .

* masaaki@nucl.sci.hokudai.ac.jp

I. INTRODUCTION

The loss of magic numbers [1–4], which occurs in unstable nuclei with neutron numbers $N = 8, 20, 28,$ and 50 , significantly changes the structure of Fermi surface. Hence, it is expected to considerably affect the fundamental properties of nuclei, such as stability, size, and shape. In fact, decades of studies have shown that various phenomena such as nuclear deformation [5–11], shape coexistence [12–14], radius increase [15–20], and clustering [21, 22] occur with the loss of neutron magicity. The causes of the vanishing magic number, such as weak bindingness [23] and the effect of nuclear forces [24, 25], especially that of tensor force [26, 27], have also been intensively studied.

Among the neutron magic numbers, $N = 28$ is the smallest one generated by the spin-orbit interaction. Therefore, its disappearance should change the structure of the Fermi surface in a different way from the cases of $N = 8$ and 20 . More specifically, the $N = 28$ shell gap is composed of the neutron $0f_{7/2}$ and $1p_{3/2}$ orbits which belong to the same major shell in the absence of spin-orbit splitting. This means that the quenching of the $N = 28$ shell gap causes quasi-degeneracy of the orbits which have the same parity but different angular momenta by two. This will induce strong quadrupole correlations between the nucleons near the Fermi surface, which leads to various quadrupole deformation of the low-lying states [28–30]. In fact, recent accumulation of experimental data for the low-lying states and their electric transitions [31–33] are revealing the onset of the ground state deformation and the quenching of the $N = 28$ shell gap in neutron-rich Mg, Si, S and Ar isotopes. Therefore, it is important to theoretically investigate the deformation of each isotopes and provide an insight to the mechanism behind it.

For this purpose, we apply the theoretical framework of antisymmetrized molecular dynamics (AMD) [22, 34, 35] to the neutron-rich Mg, Si, S and Ar isotopes. We present their energy surfaces and single-particle levels as functions of the quadrupole deformation parameters. We also provide the excitation spectra and electric properties of the low-lying states to compare with the observed data. It will be shown that the interplay between the proton and neutron shell effects strongly affects the shape of the $N = 28$ isotones and induces the γ deformation of the $N = 26$ and 30 isotones. The analysis of the neutron occupation number shows that the erosion of the $N = 28$ magicity gradually occurs and there is no definite boundaries in nuclear chart where the magicity of $N = 28$ is lost. It is also found that there

are two different patterns in the $N = 28$ magicity loss.

This paper is organized as follows. In the next section, we briefly explain the framework of AMD. In the section III, we present the numerical results for $N = 26, 28$ and 30 isotones; the energy surfaces, single-particle levels, neutron occupation numbers, spectra and electric properties. Based on these numerical data, we will discuss the factors that determine the shape of each nucleus and the relationship to the loss of the neutron magic number. Final section summarizes this work.

II. THEORETICAL FRAMEWORK

The A -body Hamiltonian used in this study is given as,

$$\hat{H} = \sum_i^A \hat{t}_i - \hat{t}_{\text{cm}} + \frac{1}{2} \sum_{ij}^A \hat{v}_{ij}^{\text{NN}} + \frac{1}{2} \sum_{ij \in \text{proton}}^Z \hat{v}_{ij}^{\text{C}}, \quad (1)$$

where the Gogny D1S density functional [36] is employed as an effective nucleon-nucleon interaction \hat{v}_{ij}^{NN} and the Coulomb interaction \hat{v}_{ij}^{C} is approximated by a sum of seven Gaussians. The center-of-mass kinetic energy \hat{t}_{cm} is exactly removed.

The variational wave function is a parity-projected Slater determinant,

$$\Phi^\pi = \hat{P}^\pi \mathcal{A}\{\varphi_1, \varphi_2, \dots, \varphi_A\}, \quad (2)$$

where \hat{P}^π is the parity projection operator. In this study, we investigate the low-lying positive-parity states. The single-particle wave packet φ_i is represented by a deformed Gaussian wave packet [37],

$$\varphi_i(\mathbf{r}) = \exp \left\{ - \sum_{\sigma=x,y,z} \nu_\sigma (r_\sigma - Z_{i\sigma})^2 \right\} \chi_i \eta_i, \quad (3)$$

$$\chi_i = a_i \chi_\uparrow + b_i \chi_\downarrow, \quad \eta_i = \{ \text{proton or neutron} \}. \quad (4)$$

The variational parameters are the width (ν_x, ν_y, ν_z) and the centroids \mathbf{Z}_i of Gaussian wave packets; and spin direction a_i and b_i . They are determined by the variation with the constraint on the matter quadrupole deformation parameters β and γ [38]. The sum of the energy and the constraint potentials,

$$\begin{aligned} \tilde{E}^\pi(\beta, \gamma) &= \frac{\langle \Phi^\pi(\beta, \gamma) | \hat{H} | \Phi^\pi(\beta, \gamma) \rangle}{\langle \Phi^\pi(\beta, \gamma) | \Phi^\pi(\beta, \gamma) \rangle} \\ &+ v_\beta (\langle \beta \rangle - \beta)^2 + v_\gamma (\langle \gamma \rangle - \gamma)^2. \end{aligned} \quad (5)$$

is minimized to obtain the optimized wave function $\Phi^\pi(\beta, \gamma)$ for given values of β and γ . The strengths of the constraint v_β and v_γ are chosen sufficiently large. In this study, the set of (β, γ) is chosen on the triangular lattice on the β - γ plane ranging from $\beta = 0$ to 0.6 with interval of 0.05.

After the variational calculation, we perform the angular momentum projection and the generator coordinate method (GCM). The optimized wave functions are projected to the eigenstate of the angular momentum,

$$\Phi_{MK}^{J\pi}(\beta_i, \gamma_i) = \frac{2J+1}{8\pi^2} \int d\Omega D_{MK}^{J*}(\Omega) \hat{R}(\Omega) \Phi^\pi(\beta_i, \gamma_i), \quad (6)$$

where $D_{MK}^J(\Omega)$ and $R(\Omega)$ represent the Wigner's D function and rotation operator. The projected wave functions are superposed employing β and γ as the generator coordinates,

$$\Psi_{M\alpha}^{J\pi} = \sum_{iK} g_{iK\alpha} \Phi_{MK}^{J\pi}(\beta_i, \gamma_i), \quad (7)$$

where the coefficients $g_{iK\alpha}$ and eigenenergies E_α are obtained by solving the Hill-Wheeler equation [39],

$$\sum_{jK'} H_{iKjK'} g_{jK'\alpha} = E_\alpha \sum_{jK'} N_{iKjK'} g_{jK'\alpha}, \quad (8)$$

$$H_{iKjK'} = \langle \Phi_{MK}^{J\pi}(\beta_i, \gamma_i) | \hat{H} | \Phi_{MK'}^{J\pi}(\beta_j, \gamma_j) \rangle, \quad (9)$$

$$N_{iKjK'} = \langle \Phi_{MK}^{J\pi}(\beta_i, \gamma_i) | \Phi_{MK'}^{J\pi}(\beta_j, \gamma_j) \rangle. \quad (10)$$

In order to discuss the breaking of the magic number, we also calculate the single-particle configuration of the optimized wave function by the following procedure [40]. We first transform the single-particle wave packets φ_i into the orthonormalized basis $\tilde{\varphi}_p$,

$$\tilde{\varphi}_p = \frac{1}{\sqrt{\mu_p}} \sum_i c_{ip} \varphi_i, \quad (11)$$

where μ_p and c_{ip} are the eigenvalues and the eigenvectors of the overlap matrix B ,

$$\sum_j B_{ij} c_{jp} = \mu_p c_{ip}, \quad B_{ij} = \langle \varphi_i | \varphi_j \rangle. \quad (12)$$

With this basis, the single-particle Hamiltonian is defined as,

$$\begin{aligned} h_{pq} = & \langle \tilde{\varphi}_p | \hat{t} | \tilde{\varphi}_q \rangle + \sum_r \langle \tilde{\varphi}_p \tilde{\varphi}_r | \hat{v}^{\text{NN}} + \hat{v}^{\text{C}} | \tilde{\varphi}_q \tilde{\varphi}_r - \tilde{\varphi}_r \tilde{\varphi}_q \rangle \\ & + \frac{1}{2} \sum_{r,s} \langle \tilde{\varphi}_r \tilde{\varphi}_s | \tilde{\varphi}_p^* \tilde{\varphi}_q \frac{\delta \hat{v}^{\text{NN}}}{\delta \rho} | \tilde{\varphi}_r \tilde{\varphi}_s - \tilde{\varphi}_s \tilde{\varphi}_r \rangle. \end{aligned} \quad (13)$$

The eigenvalues and eigenvectors of h_{pq} give the single-particle energies ϵ_p and wave functions ϕ_α ,

$$\sum_q h_{pq} f_{q\alpha} = \epsilon_\alpha f_{p\alpha}, \quad (14)$$

$$\phi_\alpha = \sum_p f_{p\alpha} \tilde{\varphi}_p = \sum_i \left(\sum_p c_{ip} \frac{1}{\sqrt{\mu_p}} f_{p\alpha} \right) \varphi_i. \quad (15)$$

III. RESULTS AND DISCUSSION

A. ground state deformation, Fermi levels and $N = 28$ magicity

Figure 1 (a) shows the energy surfaces of $N = 26, 28$ and 30 isotones as functions of the deformation parameters β and γ obtained by the angular momentum projection to $J^\pi = 0^+$. It shows that all nuclei including the $N = 28$ isotones have deformed energy minima (filled circles in Fig. 1 (a)) whose deformation parameter β are larger than 0.2 . This implies that the magicity of the neutron number $N = 28$ is lost in this mass region. Furthermore, the energy surfaces are quite soft against γ deformation and most of the energy minima are triaxially deformed. For example, the energy minimum of ^{44}Ar is at $(\beta, \gamma) = (0.26, 30^\circ)$ and triaxially deformed, but its energy is very close to the prolate and oblate deformed states with $(\beta, \gamma) = (0.26, 0^\circ)$ and $(0.26, 60^\circ)$ which are only 1.5 and 1.6 MeV above the triaxial state, respectively. We note that the angular momentum projection is essentially important to describe triaxial deformation. Before the projection, all nuclei except for ^{38}Mg and ^{46}S have axially deformed minima indicated by triangles in the figure, but after the projection, triaxially deformed states gain larger binding energy and become the ground state. We also note that ^{40}Mg , ^{42}Mg , ^{40}Si and ^{44}S have low-lying local energy minima (open circles in Fig. 1 (a)) at $2.8, 2.8, 1.2$ and 0.19 MeV above the global minima, which generate the low-lying 0_2^+ states.

In order to evaluate the deformation of individual nuclei in detail, we calculate the squared GCM amplitude which is the overlap between a basis wave function (Eq. (6)) with the deformation parameters (β, γ) and a GCM wave function (Eq. (7)),

$$O_K^{J^\pi}(\beta, \gamma) = |\langle \Phi_{MK}^{J^\pi}(\beta, \gamma) | \Psi_{M\alpha}^{J^\pi} \rangle|^2. \quad (16)$$

Larger amplitude means larger probability for corresponding values of the deformation pa-

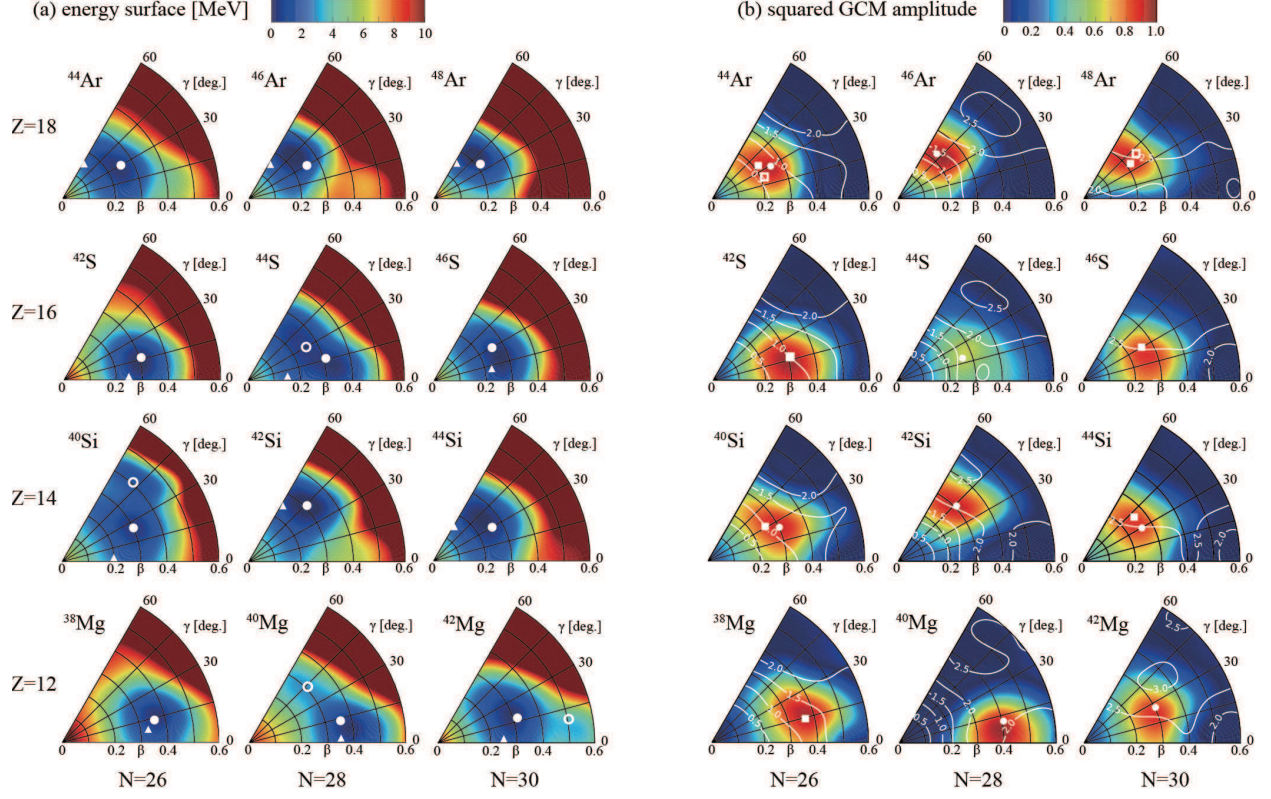


FIG. 1. (a) Energy surfaces of the $J^\pi = 0^+$ states as functions of the quadrupole deformation parameters β and γ . The filled (open) circles show the global (local) minima. Color plots show the energies relative to the global minima. The triangles show the energy minima before the angular momentum projection. (b) Squared GCM amplitude (color plots) and occupation number of the $1p$ orbit (contour lines) of the ground state. The filled circles and squares show the maxima of the squared GCM amplitudes for the ground and 2_1^+ states, while open squares show the maximum for the 2_2^+ state of $N = 26$ and 30 isotones.

rameters (β , γ), and its maximum may be regarded as the most probable intrinsic shape. The calculated amplitudes for the ground states are shown in Fig. 1 (b). They show that the ground states of almost all nuclei largely overlap with triaxially deformed shape with $15^\circ < \gamma < 45^\circ$, and their maxima (filled circles) are close to the minima of the energy surfaces shown in Fig. 1 (a). Because of triaxial deformation, the $N = 26$ and 30 isotones have the non-yrast $K^\pi = 2^+$ bands built on the 2_2^+ states as discussed later. Figure 1 also show a trend that the Ar and Si isotopes favor the oblate shape ($\gamma > 30^\circ$), while S and Mg isotopes are prolate shaped ($\gamma < 30^\circ$).

To understand the origin of the shape of each nuclei, Fig. 2 shows the proton and neutron

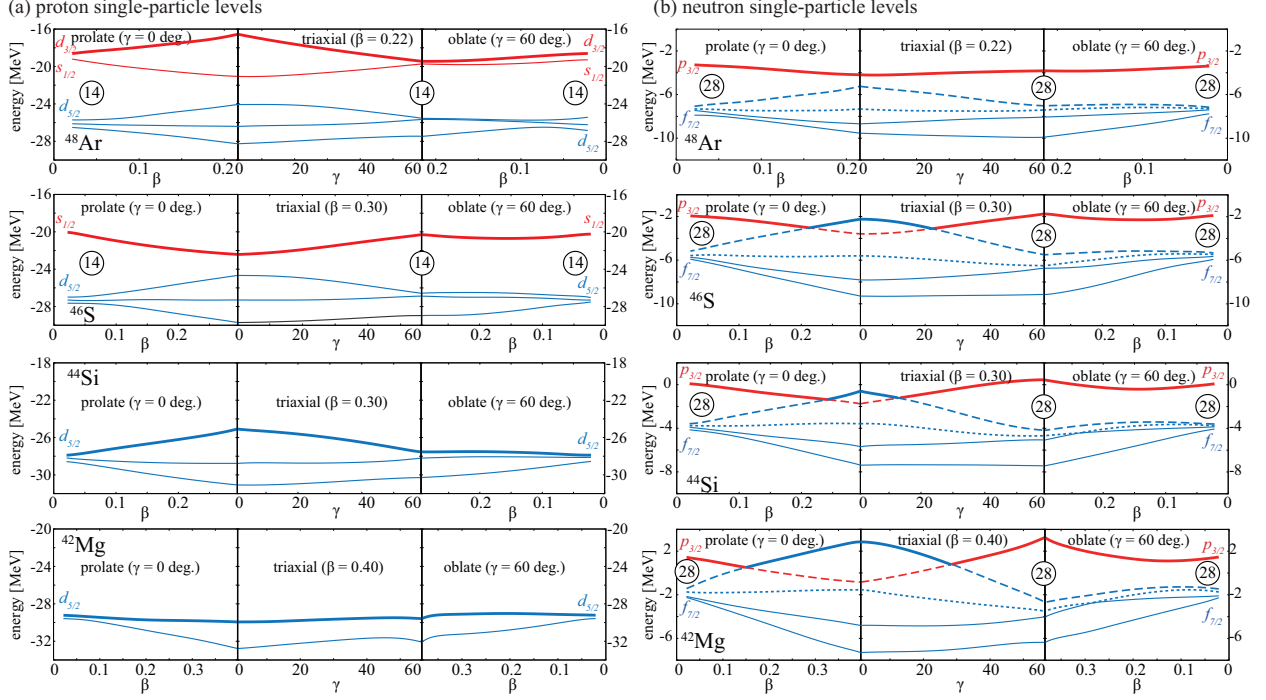


FIG. 2. (a) Proton single particle levels of the $N = 30$ isotones as functions of the quadrupole deformation parameters. Left (right) panels describe prolate (oblate) deformation, while the middle panels describe triaxial deformation. Bold lines show the highest occupied orbits. (b) Same with the panels (a), but for neutrons. Bold, dashed and dotted lines show the highest occupied orbits of the $N = 26, 28$ and 30 isotones.

single-particle orbits of the $N = 30$ isotones as functions of the quadrupole deformation parameters. We note that $N = 26$ and 28 isotones have qualitatively the same structure of single-particle orbits. First, we focus on the proton Fermi level (highest occupied orbit) shown by bold lines in panel (a). In Ar and Si, its energy is lowered by oblate deformation, which explains the reason why these isotopes tend to manifest oblate deformation. On the other hand, in S and Mg, the Fermi level is lowered by prolate deformation or almost flat. Thus, the proton Fermi level causes the general deformation trend of each isotope.

The neutron single-particle orbits show the different dependence on deformation. The neutron Fermi level of the $N = 30$ isotones (bold lines in panel (b)) is almost constant in Ar, but as proton number decreases, it starts to show deformation dependence. This partly owes to the quench of $N = 28$ shell gap and resultant level inversion. They induce many-body correlation leading to the rearrangement of the single-particle levels in a self-

consistent manner. Note that the spherical $N = 28$ shell-gap gets smaller as the proton number decreases. It is 4.0, 3.5, 3.4 and 2.8 MeV for ^{48}Ar , ^{46}S , ^{44}Si and ^{42}Mg , respectively. Consequently, ^{42}Mg is strongly suffered from the shell quenching and results in the bumpy behavior of the Fermi level. The Fermi levels of the $N = 28$ isotones (dashed lines in panel (b)) more clearly depend on deformation and tend to favor oblate deformation except for Mg. Similarly to the $N = 30$ isotones, the deformation dependence gets stronger as proton number decreases. In contrast to $N = 28$ and 30 isotones, the Fermi levels of $N = 26$ isotones show moderate dependence (dotted lines in panel (b)) as they are well below the $N = 28$ shell gap and more deeply bound.

The interplay between the proton and neutron shell effects affects the shape of $N = 28$ isotones. Let us explain it with a couple of examples. In the case of ^{42}Si , both proton and neutron Fermi levels favor the oblate shape and coherently induce strong oblate deformation. Similarly, the proton and neutron shell effects cooperatively bring about oblate deformation to ^{46}Ar and prolate deformation to ^{40}Mg . To the contrary, the proton and neutron shell effect act in the opposite way for ^{44}S ; proton's Fermi level favors prolate deformation whereas the neutron's one favors oblate deformation. As a result, the energy surface of ^{44}S is double-well shaped with two minima in prolate and oblate sides, and the many body correlation induced on top it makes the low-lying spectrum of ^{44}S rather complex compared to neighboring nuclei. Indeed, many low-lying non-yrast states have been observed [41, 42] in this nucleus and their unique nature has been discussed [43, 44].

As mentioned above, most of the $N = 26$ and 30 isotones have flat neutron Fermi levels insensitive to deformation, so their energy surfaces are also flat to deformation. This activates the degree-of-freedom of γ deformation and generates the low-lying $K^\pi = 2^+$ bands to be discussed in the next section. An exceptional case is ^{42}Mg in which neutron Fermi level shows bumpy behavior due to the quenched $N = 28$ shell gap and level inversion. At $\gamma = 30^\circ$, the neutron Fermi energy is low and high single-particle level density induces pairing correlations to gain larger binding energy. Consequently, ^{42}Mg has a well-developed triaxially deformed energy minimum. Another point mentioned for this nucleus is that it is not bound by the Gogny D1S density functional used in this study. This result contradicts to the recent shell model study [45], and hence, the experimental information on the binding of this nucleus will give us a deeper understanding of nuclear force.

The last issue to mention in Fig. 2 is the loss of the $N = 28$ magicity. In the prolate

deformed region, the level inversion takes place between the neutron single-particle levels which originate in the spherical $0f_{7/2}$ and $1p_{3/2}$. In the case of the $N = 30$ isotones, it occurs at $\beta=0.22, 0.24$ and 0.15 in ^{46}S , ^{44}Si and ^{42}Mg , respectively. On the other hand, the $N = 28$ shell gap is kept large in the oblate deformed region, and hence, we are tempted to conclude that the magicity of the neutron number 28 is robust in the oblate deformed nuclei such as ^{42}Si . However, as we show below, the $N = 28$ magicity is also lost in oblate and triaxial deformed nuclei even though there is no explicit inversion of the single-particle levels. To elucidate this, we consider the multipole decomposition of the single-particle orbits (Eq. (15)) as,

$$\phi_i(\mathbf{r}) = \sum_{jlj_z} \phi_{i;jlj_z}(r)[Y_l(\hat{r}) \times \chi_{1/2}]_{jj_z}. \quad (17)$$

The squared integral of the $l = 1$ components ($p_{3/2}$ and $p_{1/2}$) gives us an estimate of the occupation number of the neutron $1p$ -orbit. Assuming the complete filling of the $0p$ -orbit, the neutron occupation number of the $1p$ -orbit is obtained as,

$$N_{1p} = \sum_{i=1}^N \sum_{jj_z} \int_0^\infty |r\phi_{i;j1j_z}(r)|^2 dr - 6. \quad (18)$$

The contours in Fig. 1 (b) show the occupation numbers of the $1p$ orbits as functions of the deformation parameters. It must be noted that the occupation number becomes large not only in the prolate deformed region but also in the oblate deformed region even though there is no single-particle level inversion. This indicates that the deformation causes the strong mixing of the $l = 3$ and 1 components in the single-particle levels close to the Fermi surface to increase the p -wave occupation probability. Consequently, there are two different types in the loss of the $N = 28$ magicity: The magicity is lost due the single-particle level inversion in the prolate deformed nuclei, while it is lost without the inversion in the oblate deformed nuclei.

The maximum of the GCM amplitude of $N = 28$ isotones ($^{42}\text{Ar}, ^{44}\text{S}, ^{42}\text{Si}$ and ^{40}Mg) are located at the regions where the occupation number is close to or larger than 2. Therefore, their ground states are dominated by the $2p2h$ configurations because of the loss of the $N = 28$ magicity. To illustrate the landscape of the magicity loss, Fig. 3 shows the occupation number of the $1p$ orbits at the maximum of the GCM amplitudes. It shows that the occupation number gradually and continuously increases as proton number decreases and

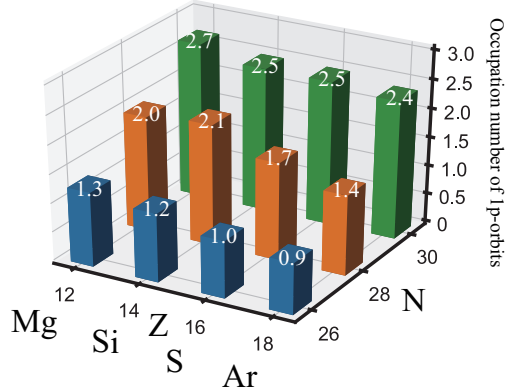


FIG. 3. Occupation number of the neutron $1p$ orbits at the position where the GCM amplitude of the ground state is maximum.

neutron number increases. Therefore, it seems that there is no clear boundary in nuclear chart where the $N = 28$ magicity is lost. This feature is different from the case of the island of inversion which seems to have distinct boundary at $N = 19$ and $Z = 13$ [5, 46–48].

B. Low-lying spectrum and triaxial deformation

Here, we discuss how quadrupole deformation, in particular the γ deformation, influences to the excitation spectrum. Figure 4 shows the energy spectra obtained by the GCM calculations which are labeled as “triaxial”. Compared to a closed-shell nucleus ^{48}Ca which has the 2_1^+ and 4_1^+ states at 3.8 MeV and 4.5 MeV [51], all of the calculated Mg, Si, S and Ar isotopes have low-lying 2_1^+ and 4_1^+ states, and the energy ratios $E(4_1^+)/E(2_1^+)$ are close to 3.3, indicating their rotational nature. These characteristics are consistent with the observed spectra, although the calculation overestimates the moments-of-inertia of several nuclei. Because of the deformation, the $E2$ transition strengths ($0_1^+ \rightarrow 2_1^+$) listed in table I are stronger than $200 e^2\text{fm}^4$ in all nuclei which are more than twice as large as that of ^{48}Ca [52]. All these results are in accordance with the loss of the $N = 28$ magicity.

In addition to the rotational ground band, all the $N = 26$ and 30 isotones have the low-lying non-yrast $K^\pi = 2^+$ bands built on the 2_2^+ states because of their pronounced triaxial deformation. Note that the maximum GCM amplitudes of the 2_1^+ and 2_2^+ states (squares and triangles in Fig. 1 (b)) are located at almost the same position showing that the intrinsic shape of the ground band and $K^\pi = 2^+$ band are similar to each other. Experimentally,

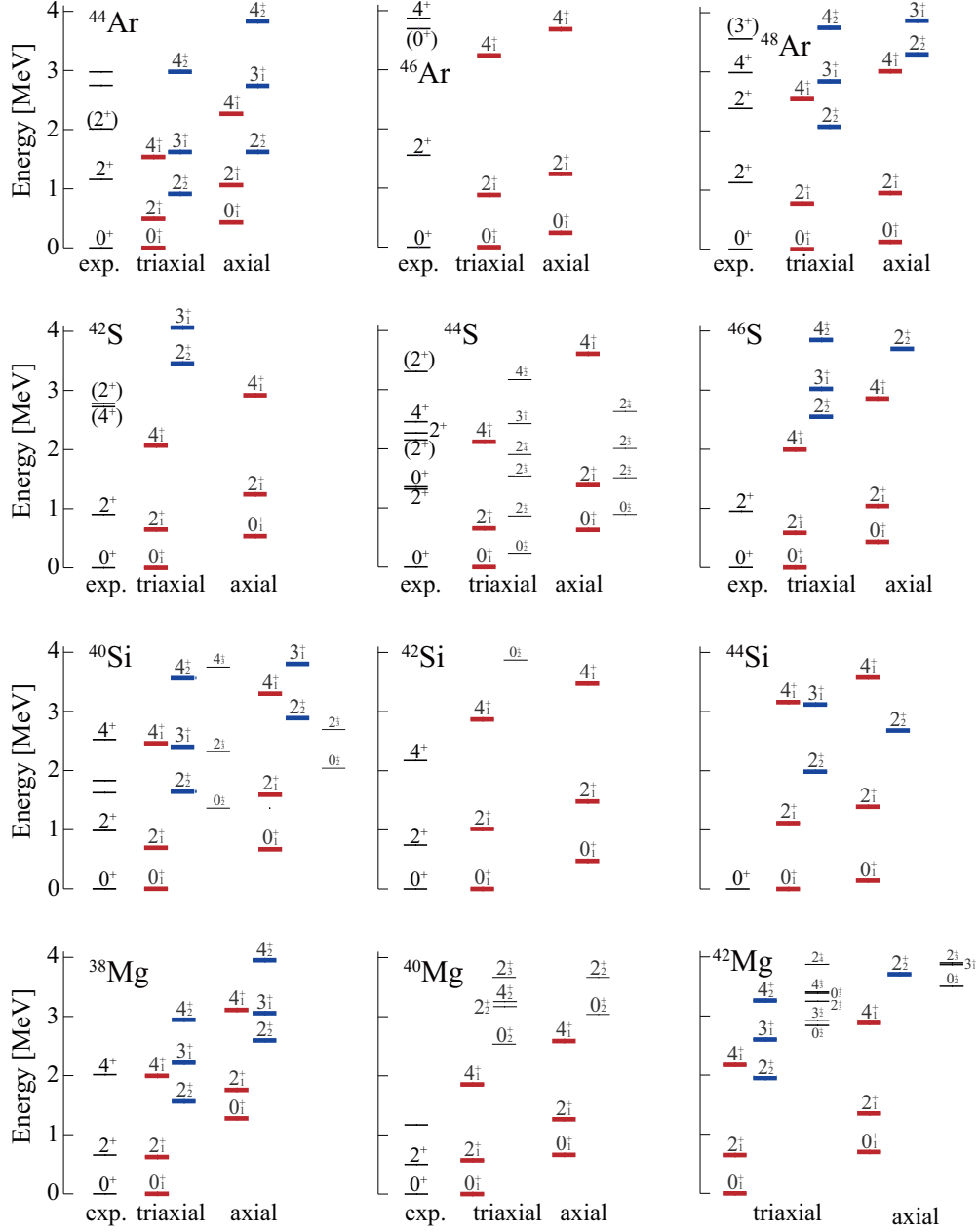


FIG. 4. Low-lying positive-parity spectra of the $N = 26, 28$ and 30 isotones up to $J^\pi = 4^+$ compared to the experimental data. “triaxial” denotes the results of the GCM calculations which allow γ deformation, while “axial” denotes that limited to axial symmetric shape ($\gamma = 0^\circ$ or 60°).

the candidates of the 2_2^+ state have been observed in ^{40}Si , ^{42}S , ^{44}Ar and ^{48}Ar . The small excitation energies of the 3^+ state as a member of the $K^\pi = 2^+$ band is another signature of triaxial deformation. The candidates such 3^+ state have also been observed at 4.2 MeV in ^{42}S and 3.3 MeV in ^{48}Ar .

TABLE I. The calculated and observed $B(E2)$ strengths in the unit of $e^2\text{fm}^4$ and electric quadrupole moments in the unit of efm^2 . “triaxial” denotes the results obtained by the GCM calculations which allow γ deformation, while “axial” denotes that restricted to axial symmetric shape.

		^{38}Mg	^{40}Si	^{42}S	^{44}Ar	^{40}Mg	^{42}Si	^{44}S	^{46}Ar	^{42}Mg	^{44}Si	^{46}S	^{48}Ar
$B(E2; 0_1^+ \rightarrow 2_1^+)$	triaxial	440	209	406	231	486	365	383	334	341	221	359	346
	axial	357	162	416	286	474	356	145	326	290	194	326	321
	exp.			397^{+63}_{-63}	378^{+34}_{-55}			314^{+88}_{-88}	216^{+22}_{-22} [49]				
		570^{+335}_{-160} [50]											
$B(E2; 0_1^+ \rightarrow 2_2^+)$	triaxial	18	90	58	88	0.03		8.4		26	15	89	7.1
	axial	9.8	40	14	6.0	0.06		10		4.1	7.9	36	1.4
	exp.				23^{+2}_{-2}								
$B(E2; 2_1^+ \rightarrow 2_2^+)$	triaxial	11	45	14	72	0.02		2.5		11	68	14	17
	axial	0.2	16	3.5	42	0.07		14		9.6	53	7.3	2.2
	exp.				680^{+150}_{-90}								
$Q(2_1^+)$	triaxial	-18.5	-10.3	-18.4	-7.0	-20.1	17.3	-18.0	16.8	-16.3	2.1	-18.1	15.8
	axial	-17.4	-6.4	-18.7	11.5	-19.6	17.6	-12.1	16.5	-15.0	5.3	-17.0	16.4
	exp.				-8.3^{+3}_{-3}								

To investigate how the degrees of γ deformation affect the low-lying spectroscopy, we have performed additional GCM calculations which are restricted to axial deformation. The obtained spectra are labeled as “axial” in Fig. 4. It is found that the energy of the non-yrast bands is sensitive to the degrees of γ deformation. Namely, the $K^\pi = 2^+$ bands of the $N = 26$ and 30 isotones calculated by the axial GCM are much less bound than the triaxial results. On the other hand, the energies of the ground states are not strongly affected by the degree of triaxial deformation except for ^{38}Mg . The axial and triaxial GCM calculations also yielded largely different inter-band transition strengths between the ground and $K^\pi = 2^+$ bands as listed in Table I. The $0_1^+ \rightarrow 2_2^+$ and $2_1^+ \rightarrow 2_2^+$ transitions obtained by the axial GCM are much smaller than those obtained by the triaxial GCM except for ^{44}Si . In short, the degree-of-freedom of γ deformation is mostly reflected to the properties of the non-yrast

$K^\pi = 2^+$ band. We also remark that the triaxial GCM reproduces the quadrupole moment of the 2_1^+ states of ^{44}Ar while the axial GCM does not. Thus, the electric quadrupole transitions and moments are sensitive probes for the triaxial deformation. In particular, the properties of the non-yrast $K^\pi = 2^+$ band is important to identify the triaxial deformation of the $N = 26$ and 30 isotones.

IV. SUMMARY

In this work, we aimed to investigate the nature and cause of the nuclear deformations and its relation to the loss of the neutron magicity $N = 28$ in vicinity of ^{42}Si . For this purpose, we have employed a theoretical framework of AMD combined with the Gogny D1S density functional to calculate the neutron-rich $N = 26, 28$ and 30 isotones. We have presented the energy surfaces, GCM amplitudes and single-particle levels as functions of the quadrupole deformation parameters. We have also shown the spectra and electric properties of the low-lying states, which qualitatively agree with the observed data and predict the existence of the many non-yrast states.

The analysis of the energy surfaces and the single particle levels has revealed that the interplay between the proton and neutron shell effects strongly affects shape of the $N = 28$ isotones. In the case of ^{46}Ar , ^{42}Si and ^{40}Mg , they cooperatively act and induce oblate or prolate deformation. On the other hand, they act in the opposite way and make the double-well shaped energy surface of ^{44}S . Consequently, the low-lying spectrum of ^{44}S is relatively complicated and many a couple of 2^+ states coexist within small excitation energy. In the case of the $N = 26$ and 30 isotones, except for ^{42}Mg , the neutron Fermi level is insensitive to deformation. As a result, the energy surfaces become quite soft against γ deformation, and many of the $N = 26$ and 30 isotones have the triaxially deformed ground states. We have pointed out that the triaxial deformation of the $N = 26$ and 30 isotones is mostly reflected in the properties of the non-yrast $K^\pi = 2^+$ bands, especially in their inter-band $E2$ transition strengths.

Finally, we note that the erosion of the $N = 28$ magicity gradually occurs as seen in the occupation number of the neutron $1p$ orbits. Therefore, there is no definite boundaries in nuclear chart where the magicity of $N = 28$ is lost. This is unlike to the case of the magic number $N = 20$ (island of inversion). We also remark that there are two different patterns

of the $N = 28$ magicity loss. In the case of the prolate deformed nuclei such as ^{42}Mg , the magicity is lost by the inversion of single-particle levels, while it is lost without the inversion in the case of the oblate deformed nuclei such as ^{42}Si . In the forthcoming paper, we will revisit this issue and discuss how to distinguish these two patterns experimentally.

ACKNOWLEDGMENTS

One of the author (M.K.) acknowledges that this work was supported by the JSPS KAKENHI Grant No. 19K03859 and by the COREnet program at RCNP Osaka University. Part of the numerical calculations were performed using Oakforest-PACS at the Center for Computational Sciences in the University of Tsukuba.

-
- [1] D. H. Wilkinson and D. E. Alburger, *Physical Review* **113**, 563 (1959).
 - [2] I. Talmi and I. Unna, *Physical Review Letters* **4**, 469 (1960).
 - [3] C. Thibault, R. Klapisch, C. Rigaud, A. M. Poskanzer, R. Prieels, L. Lessard, and W. Reisdorf, *Physical Review C* **12**, 644 (1975).
 - [4] O. Sorlin and M.-G. G. Porquet, *Progress in Particle and Nuclear Physics* **61**, 602 (2008).
 - [5] E. K. Warburton, J. A. Becker, and B. A. Brown, *Physical Review C* **41**, 1147 (1990).
 - [6] N. Fukunishi, T. Otsuka, and T. Sebe, *Physics Letters B* **296**, 279 (1992).
 - [7] T. Motobayashi, Y. Ikeda, K. Ieki, M. Inoue, N. Iwasa, T. Kikuchi, M. Kurokawa, S. Moriya, S. Ogawa, H. Murakami, S. Shimoura, Y. Yanagisawa, T. Nakamura, Y. Watanabe, M. Ishihara, T. Teranishi, H. Okuno, and R. F. Casten, *Physics Letters B* **346**, 9 (1995).
 - [8] O. Sorlin, D. Guillemaud-Mueller, A. C. Mueller, V. Borrel, S. Dogny, F. Pougheon, K. L. Kratz, H. Gabelmann, B. Pfeiffer, A. Wöhr, W. Ziegert, Y. E. Penionzhkevich, S. M. Lukyanov, V. S. Salamatin, R. Anne, C. Borcea, L. K. Fifield, M. Lewitowicz, M. G. Saint-Laurent, D. Bazin, C. Détraz, F. K. Thielemann, and W. Hillebrandt, *Physical Review C* **47**, 2941 (1993).
 - [9] H. Scheit, T. Glasmacher, B. A. Brown, J. A. Brown, P. D. Cottle, P. G. Hansen, R. Harkewicz, M. Hellström, R. W. Ibbotson, J. K. Jewell, K. W. Kemper, D. J. Morrissey, M. Steiner, P. Thiof, and M. Thoennessen, *Physical Review Letters* **77**, 3967 (1996).

- [10] T. Glasmacher, B. A. Brown, M. J. Chromik, P. D. Cottle, M. Fauerbach, R. W. Ibbotson, K. W. Kemper, D. J. Morrissey, H. Scheit, D. W. Sklenicka, and M. Steiner, *Physics Letters, Section B: Nuclear, Elementary Particle and High-Energy Physics* **395**, 163 (1997).
- [11] S. Takeuchi, M. Matsushita, N. Aoi, P. Doornenbal, K. Li, T. Motobayashi, H. Scheit, D. Steppebeck, H. Wang, H. Baba, D. Bazin, L. C aceres, H. Crawford, P. Fallon, R. Gernh user, J. Gibelin, S. Go, S. Gr vy, C. Hinke, C. R. Hoffman, R. Hughes, E. Ideguchi, D. Jenkins, N. Kobayashi, Y. Kondo, R. Kr ucken, T. Le Bleis, J. Lee, G. Lee, A. Matta, S. Michimasa, T. Nakamura, S. Ota, M. Petri, T. Sako, H. Sakurai, S. Shimoura, K. Steiger, K. Takahashi, M. Takechi, Y. Togano, R. Winkler, and K. Yoneda, *Physical Review Letters* **109**, 182501 (2012).
- [12] K. Heyde and J. L. Wood, *Reviews of Modern Physics* **83**, 1467 (2011).
- [13] T. Otsuka and Y. Tsunoda, *Journal of Physics G* **43**, 18 (2016).
- [14] H. Nishibata, S. Kanaya, T. Shimoda, A. Odahara, S. Morimoto, A. Yagi, H. Kanaoka, M. R. Pearson, C. D. Levy, M. Kimura, N. Tsunoda, and T. Otsuka, *Physical Review C* **99**, 024322 (2019).
- [15] I. Tanihata, H. Hamagaki, O. Hashimoto, Y. Shida, N. Yoshikawa, K. Sugimoto, O. Yamakawa, T. Kobayashi, and N. Takahashi, *Physical Review Letters* **55**, 2676 (1985).
- [16] A. Ozawa, T. Suzuki, and I. Tanihata, *Nuclear Physics A* **693**, 32 (2001).
- [17] W. Horiuchi and Y. Suzuki, *Physical Review C* **74**, 034311 (2006).
- [18] T. Nakamura, N. Kobayashi, Y. Kondo, Y. Satou, N. Aoi, H. Baba, S. Deguchi, N. Fukuda, J. Gibelin, N. Inabe, M. Ishihara, D. Kameda, Y. Kawada, T. Kubo, K. Kusaka, A. Mengoni, T. Motobayashi, T. Ohnishi, M. Ohtake, N. A. Orr, H. Otsu, T. Otsuka, A. Saito, H. Sakurai, S. Shimoura, T. Sumikama, H. Takeda, E. Takeshita, M. Takechi, S. Takeuchi, K. Tanaka, K. N. Tanaka, N. Tanaka, Y. Togano, Y. Utsuno, K. Yoneda, A. Yoshida, and K. Yoshida, *Physical Review Letters* **103**, 262501 (2009).
- [19] M. Takechi, T. Ohtsubo, M. Fukuda, D. Nishimura, T. Kuboki, T. Suzuki, T. Yamaguchi, A. Ozawa, T. Moriguchi, H. Ooishi, D. Nagae, H. Suzuki, S. Suzuki, T. Izumikawa, T. Sumikama, M. Ishihara, H. Geissel, N. Aoi, R. J. Chen, D. Q. Fang, N. Fukuda, I. Hachi-uma, N. Inabe, Y. Ishibashi, Y. Ito, D. Kameda, T. Kubo, K. Kusaka, M. Lantz, Y. G. Ma, K. Matsuta, M. Mihara, Y. Miyashita, S. Momota, K. Namihira, M. Nagashima, Y. Ohkuma, T. Ohnishi, M. Ohtake, K. Ogawa, H. Sakurai, Y. Shimbara, T. Suda, H. Takeda, S. Takeuchi,

- K. Tanaka, R. Watanabe, M. Winkler, Y. Yanagisawa, Y. Yasuda, K. Yoshinaga, A. Yoshida, and K. Yoshida, *Physics Letters B* **707**, 357 (2012).
- [20] K. Minomo, T. Sumi, M. Kimura, K. Ogata, Y. R. Shimizu, and M. Yahiro, *Physical Review Letters* **108**, 052503 (2012).
- [21] W. von Oertzen, M. Freer, and Y. Kanada-En'yo, *Physics Reports* **432**, 43 (2006).
- [22] M. Kimura, T. Suhara, and Y. Kanada-En'yo, *The European Physical Journal A* **52**, 373 (2016).
- [23] I. Hamamoto, *Physical Review C* **85**, 064329 (2012).
- [24] A. Poves and J. Retamosa, *Physics Letters B* **184**, 311 (1987).
- [25] E. Caurier, G. Martínez-Pinedo, F. Nowacki, A. Poves, and P. A. Zuker, *Reviews of Modern Physics* **77**, 427 (2005).
- [26] T. Otsuka, T. Suzuki, R. Fujimoto, H. Grawe, and Y. Akaishi, *Physical Review Letters* **95**, 232502 (2005).
- [27] T. Otsuka, A. Gade, O. Sorlin, T. Suzuki, and Y. Utsuno, *Reviews of Modern Physics* **92**, 015002 (2020).
- [28] D. Santiago-Gonzalez, I. Wiedenhöver, V. Abramkina, M. L. Avila, T. Baugher, D. Bazin, B. A. Brown, P. D. Cottle, A. Gade, T. Glasmacher, K. W. Kemper, S. McDaniel, A. Rojas, A. Ratkiewicz, R. Meharchand, E. C. Simpson, J. A. Tostevin, A. Volya, and D. Weisshaar, *Physical Review C* **83**, 061305 (2011).
- [29] Y. Utsuno, T. Otsuka, B. A. Brown, M. Honma, T. Mizusaki, and N. Shimizu, *Physical Review C* **86**, 1 (2012), arXiv:1210.5469.
- [30] M. Kimura, Y. Taniguchi, Y. Kanada-En'yo, H. Horiuchi, and K. Ikeda, *Physical Review C - Nuclear Physics* **87**, 1 (2013).
- [31] T. Mijatović, N. Kobayashi, H. Iwasaki, D. Bazin, J. Belarge, P. C. Bender, B. A. Brown, A. Dewald, R. Elder, B. Elman, A. Gade, M. Grindler, T. Haylett, S. Heil, C. Loelius, B. Longfellow, E. Lunderberg, M. Mathy, K. Whitmore, and D. Weisshaar, *Physical Review Letters* **121**, 012501 (2018).
- [32] S. Momiyama, K. Wimmer, D. Bazin, J. Belarge, P. Bender, B. Elman, A. Gade, K. W. Kemper, N. Kitamura, B. Longfellow, E. Lunderberg, M. Niikura, S. Ota, P. Schrock, J. A. Tostevin, and D. Weisshaar, *Physical Review C* **102**, 034325 (2020).
- [33] B. Longfellow, D. Weisshaar, A. Gade, B. A. Brown, D. Bazin, K. W. Brown, B. Elman,

- J. Pereira, D. Rhodes, and M. Spieker, *Physical Review Letters* **125**, 232501 (2020).
- [34] Y. Kanada-En'yo, M. Kimura, and H. Horiuchi, *Comptes Rendus Physique* **4**, 497 (2003).
- [35] Y. Kanada-En'yo, *Physical Review C - Nuclear Physics* **85**, 1 (2012), arXiv:1203.2398.
- [36] J. F. Berger, M. Girod, and D. Gogny, *Computer Physics Communications* **63**, 365 (1991).
- [37] M. Kimura, *Physical Review C* **69**, 044319 (2004).
- [38] M. Kimura, R. Yoshida, and M. Isaka, *Progress of Theoretical Physics* **127**, 287 (2012).
- [39] D. L. Hill and J. A. Wheeler, *Physical Review* **89**, 1102 (1953).
- [40] A. Doté, H. Horiuchi, and Y. Kanada-En'yo, *Physical Review C* **56**, 1844 (1997).
- [41] D. Santiago-Gonzalez, I. Wiedenhöver, V. Abramkina, M. L. Avila, T. Baugher, D. Bazin, B. A. Brown, P. D. Cottle, A. Gade, T. Glasmacher, K. W. Kemper, S. McDaniel, A. Rojas, A. Ratkiewicz, R. Meharchand, E. C. Simpson, J. A. Tostevin, A. Volya, and D. Weisshaar, *Physical Review C - Nuclear Physics* **83**, 1 (2011).
- [42] J. J. Parker, I. Wiedenhöver, P. D. Cottle, J. Baker, D. McPherson, M. A. Riley, D. Santiago-Gonzalez, A. Volya, V. M. Bader, T. Baugher, D. Bazin, A. Gade, T. Ginter, H. Iwasaki, C. Loelius, C. Morse, F. Recchia, D. Smalley, S. R. Stroberg, K. Whitmore, D. Weisshaar, A. Lemasson, H. L. Crawford, A. O. Macchiavelli, and K. Wimmer, *Physical Review Letters* **118**, 1 (2017).
- [43] T. R. Rodríguez and J. L. Egido, *Physical Review C* **84**, 1 (2011).
- [44] Y. Utsuno, N. Shimizu, T. Otsuka, T. Yoshida, and Y. Tsunoda, *Physical Review Letters* **114**, 1 (2015), arXiv:1407.0444.
- [45] N. Tsunoda, T. Otsuka, K. Takayanagi, N. Shimizu, T. Suzuki, Y. Utsuno, S. Yoshida, and H. Ueno, *Nature* **587**, 66 (2020).
- [46] R. Han, X. Q. Li, W. G. Jiang, Z. H. Li, H. Hua, S. Q. Zhang, C. X. Yuan, D. X. Jiang, Y. L. Ye, J. Li, Z. H. Li, F. R. Xu, Q. B. Chen, J. Meng, J. S. Wang, C. Xu, Y. L. Sun, C. G. Wang, H. Y. Wu, C. Y. Niu, C. G. Li, C. He, W. Jiang, P. J. Li, H. L. Zang, J. Feng, S. D. Chen, Q. Liu, X. C. Chen, H. S. Xu, Z. G. Hu, Y. Y. Yang, P. Ma, J. B. Ma, S. L. Jin, Z. Bai, M. R. Huang, Y. J. Zhou, W. H. Ma, Y. Li, X. H. Zhou, Y. H. Zhang, G. Q. Xiao, and W. L. Zhan, *Physics Letters B* **772**, 529 (2017).
- [47] K. Shimada, H. Ueno, G. Neyens, K. Asahi, D. L. Balabanski, J. M. Daugas, M. Depuydt, M. De Rydt, L. Gaudefroy, S. Grévy, Y. Hasama, Y. Ichikawa, D. Kameda, P. Morel, T. Nagatomo, L. Perrot, C. Stodel, J. C. Thomas, Y. Utsuno, W. Vanderheijden, N. Vermeulen,

- P. Vingerhoets, E. Yagi, K. Yoshida, and A. Yoshimi, *Physics Letters B* **714**, 246 (2012).
- [48] H. Heylen, M. De Rydt, G. Neyens, M. L. Bissell, L. Caceres, R. Chevrier, J. M. Daugas, Y. Ichikawa, Y. Ishibashi, O. Kamalou, T. J. Mertzimekis, P. Morel, J. Papuga, A. Poves, M. M. Rajabali, C. Stödel, J. C. Thomas, H. Ueno, Y. Utsuno, N. Yoshida, and A. Yoshimi, *Physical Review C* **94**, 034312 (2016).
- [49] S. Calinescu, L. Cáceres, S. Grévy, O. Sorlin, Z. Dombrádi, M. Stanoiu, R. Astabatyán, C. Borcea, R. Borcea, M. Bowry, W. Catford, E. Clément, S. Franchoo, R. Garcia, R. Gillibert, I. H. Guerin, I. Kuti, S. Lukyanov, A. Lepailleur, V. Maslov, P. Morfouace, J. Mrazek, F. Negoita, M. Niikura, L. Perrot, Z. Podolyák, C. Petrone, Y. Penionzhkevich, T. Roger, F. Rotaru, D. Sohler, I. Stefan, J. C. Thomas, Z. Vajta, and E. Wilson, *Physical Review C* **93**, 1 (2016).
- [50] D. Mengoni, J. J. Valiente-Dobón, A. Gadea, S. Lunardi, S. M. Lenzi, R. Broda, A. Dewald, T. Pissulla, L. J. Angus, S. Aydin, D. Bazzacco, G. Benzoni, P. G. Bizzeti, A. M. Bizzeti-Sona, P. Boutachkov, L. Corradi, F. Crespi, G. de Angelis, E. Farnea, E. Fioretto, A. Goergen, M. Gorska, A. Gottardo, E. Grodner, A. M. Howard, W. Królas, S. Leoni, P. Mason, D. Montanari, G. Montagnoli, D. R. Napoli, A. Obertelli, R. Orlandi, T. Pawlat, G. Pollarolo, F. Recchia, A. Algora, B. Rubio, E. Sahin, F. Scarlassara, R. Silvestri, J. F. Smith, A. M. Stefanini, D. Steppenbeck, S. Szilner, C. A. Ur, P. T. Wady, and J. Wrzesiński, *Physical Review C* **82**, 024308 (2010).
- [51] T. Burrows, *Nuclear Data Sheets* **107**, 1747 (2006).
- [52] T. Hartmann, J. Enders, P. Mohr, K. Vogt, S. Volz, and A. Zilges, *Physical Review C* **65**, 034301 (2002).